Journal of Power Sources 662 (2026) 238678

Contents lists available at ScienceDirect

Journal of Power Sources

journal homepage: www.elsevier.com/locate/jpowsour

# Utilising intrinsic self-protecting properties of Ni-alloys in fuel electrodes of solid oxide electrolysis cells

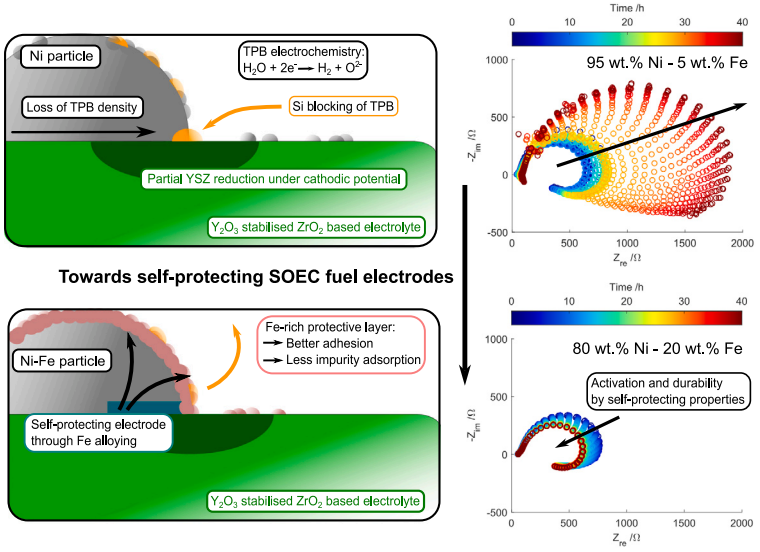
Julian Taubmann [a,b,c,*], Henrik H. Kristoffersen [b], Christodoulos Chatzichristodoulou [a], Jan Rossmeisl [b], Stephen J. Skinner [c,d], Henrik Lund Frandsen [a]

[a] Department of Energy Conversion and Storage, Technical University of Denmark, Fysikvej, Lyngby, 2800, Denmark
[b] Center of High Entropy Alloy Catalysis, Department of Chemistry, Copenhagen University, HC Ørsteds Bygningen, Copenhagen, 2100, Denmark
[c] Department of Materials, Imperial College London, Exhibition Rd, South Kensington, London SW7 2AZ, United Kingdom
[d] International Institute for Carbon-Neutral Energy Research (I2CNER), Kyushu University, Fukuoka, Japan

## HIGHLIGHTS

- Ni-alloy electrodes are analysed for their durability in solid oxide electrolysis cells.
- Cleanroom prepared NiFe and NiCu (80–20 and 95–5 wt%) electrodes are studied.
- It is found that Ni with 20 wt% Fe offers intrinsic self-protecting properties.
- Low energy ion scattering reveals the protective effect of Fe against Si impurities.
- NiMn and NiV are shown as other self-protecting alloys by density functional theory.

## GRAPHICAL ABSTRACT




## ARTICLE INFO

Dataset link: https://doi.org/10.11583/DTU.29086796.v1

*Keywords:*
Solid oxide electrolysis cell
Fuel electrode
Self-protecting electrodes
Degradation
Alloying

## ABSTRACT

The degradation of the fuel electrode composite of Ni and an oxide ion conducting oxide is a central challenge to solve for competitive long-term performance of a solid oxide electrolysis cell (SOEC) to produce green hydrogen. In this study, enhanced durability is observed using microstructural changes in Ni-alloy/$Y_2O_3$ stabilised $ZrO_2$ (YSZ) fuel electrodes as an intrinsic self-protecting mechanism. In particular, Ni–Fe alloys offer benefits through the intrinsic mobility of Fe in the alloy phase amid the application of cathodic potentials. This mobility of Fe forms protective surface layers around the Ni–Fe particles and enhances durability by: (1) preventing the loss of contact and mobility of the metal phase away from the most active reaction zones during Ni migration and (2) protecting the surface against accumulation of trace impurities of Si as a ubiquitous contaminant in $H_2O$ atmospheres. The combined approach of electrochemical testing of alloy thin-film fuel electrodes prepared by photolithography, postmortem characterisation by low-energy ion scattering (LEIS),

* Corresponding author at: Department of Energy Conversion and Storage, Technical University of Denmark, Fysikvej, Lyngby, 2800, Denmark.
*E-mail address:* julta@dtu.dk (J. Taubmann).

https://doi.org/10.1016/j.jpowsour.2025.238678
Received 25 June 2025; Received in revised form 2 September 2025; Accepted 22 October 2025
Available online 5 November 2025
0378-7753/© 2025 The Authors. Published by Elsevier B.V. This is an open access article under the CC BY license (http://creativecommons.org/licenses/by/4.0/).

X-ray photoelectron spectroscopy (XPS) and atomic force microscopy (AFM) with density functional theory (DFT) calculations is used to establish a mechanism for self-protecting electrode properties. In addition, other Ni-alloys (Ni–V, Ni–Mn) are proposed by DFT as promising electrode materials with self-protecting properties.

## 1. Introduction

Green hydrogen produced by electrolysis, using renewable electricity, is expected to play a key role in reducing $CO_2$ emissions from hard-to-abate sectors [1,2]. Considering the projected availability of resources to meet the $H_2$ targets in 2050, the efficiency of the electrolysis technology to produce $H_2$ is crucial to reduce the energy and resources needed [3]. In that context, solid oxide electrolysis cell (SOEC) technology is promising due to the high thermodynamic efficiencies (> 85%) associated with their elevated operating temperatures (600–850 °C) [4,5].

Despite such promising efficiencies, the durability of devices remains a critical challenge [4]. Such obstacles are known to a lesser extent for competitor technologies, operating at lower temperatures and with reduced efficiencies [6]. In particular, the fuel electrode traditionally a composite of Ni and an oxide ion ($O_O^\times$) conductor in $Y_2O_3$ stabilised $ZrO_2$ (YSZ), causes detrimental degradation that hampers the long-term performance of the entire cell [7,8]. In general, degradation is observed as the loss of interfacial contact between Ni/YSZ and the restructuring of Ni from the most active reaction sites [9–11], which is consequently named Ni migration [7]. Although widely researched, a common understanding and a joint hypothesis for explaining all the observations have not been achieved. In addition to Ni migration, trace impurities were repeatedly observed accumulating in the porous electrodes during operation [12,13]. These can be introduced through raw materials or be present in gas feeds supplied to the fuel electrode [12,14]. Often, impurities of the raw material are observed on the surfaces and interfaces, where they can segregate to during sintering above 1000 °C [14].

Besides the success of alloying in catalysis and electrocatalysis, when used to tune the surface reactivity [15,16], such approaches are less researched in the context of SOECs. This is despite the higher $H_2O$ splitting rate found for binary alloys of Ni ($Ni_3Me$) by density functional theory (DFT) calculations. Gu et al. suggested that alloying Ni with Fe increases the O binding strength and thereby increases the $H_2O$ splitting rate [17]. These predicted improvements were also found experimentally with porous Ni–Fe based electrodes [18]. In addition, the adhesion strength between Ni and $ZrO_2$ can be tuned by alloying of Ni, as investigated by Malyi et al. with DFT calculations [19]. There, the aim was increasing the oxygen affinity of the alloyed metal leading to a stronger adhesion between the Ni and YSZ, as was indicated for Ni–Fe and Ni–V. This was recently experimentally supported to be a route for achieving stronger Ni-alloy/YSZ interfaces less prone to contact loss with Ni–Fe and Ni–Mn alloys [20].

These studies share the aim of improving reaction rates in the electrodes or to indirectly reduce degradation rates by providing stronger interface adhesion. However, metal alloys are commonly researched in other fields (e.g., steels or other mechanical support structures, nuclear energy installations, coatings) for possible self-healing or protecting properties to repair structural damage and to extend lifetimes [21]. What is often challenging in the applications of intrinsic self-healing or self-protecting are ambient or low temperatures, limiting the mobility of atoms to diffuse to the damage site [22]. Although this commonly leads to the application of extrinsic strategies at low temperatures, a synergy of the intrinsic operating temperatures in SOECs and possible self-protecting mechanisms of the metal phase in the electrodes could exist.

Such synergies are explored in this work, envisioned to emerge between operating temperature, restructuring of the metal phase under cathodic bias and varying mobility of atoms in alloys. As model systems, we chose two widely researched Ni-alloys in Ni–Fe and Ni–Cu of two different ratios (5 and 20 wt% of Fe or Cu), respectively. Both Fe and Cu are similar in atomic radius to Ni and form stable alloys at elevated temperatures [23,24], while possessing different oxygen affinity [17]. To remove any possible microstructural effects during the preparation of porous electrodes when Fe or Cu could act as sintering aids and lead to different final microstructures, cleanroom preparation techniques such as photolithography and magnetron sputtering were used to deposit micrometre-controlled electrode patterns on YSZ substrates. The as-prepared electrode patterns are exemplified in Fig. 1 (a). The aim in this work is twofold in investigating: (1) the restructuring of the alloy phases under anodic, cathodic, and open circuit voltage (OCV), indicative of the adhesion to YSZ and (2) the possible protection against impurity accumulation from the gas-phase. A typical degradation response of a non-alloyed Ni/YSZ electrode is sketched in Fig. 1 (b).

To analyse possible effects of impurities on surfaces, low-energy ion scattering (LEIS) and X-ray photoelectron spectroscopy (XPS) are used. Microstructural investigations of the restructuring of the metal films are performed by atomic force microscopy (AFM). DFT is applied to establish a fundamental understanding of the differences between the considered Ni-alloys. The electrochemistry and defect chemistry is formulated according to the Kröger–Vink notation in the following, for example, as $H_2O + 2e' + V_O^{\cdot\cdot} \longrightarrow H_2 + O_O^\times$ with insertion of an oxide ion ($O_O^\times$) into a YSZ oxygen vacancy ($V_O^{\cdot\cdot}$).

## 2. Materials and methods

### 2.1. Model electrode sample preparation

8 mol% $Y_2O_3$ stabilised $ZrO_2$ (TZ-8Y, Tosoh, Japan) pellets were prepared as electrode substrates. The pellets were uniaxially pressed (PW 10, P-O Weber, Germany) with 50 MPa into cylindrical shape and subsequently further compacted by cold isostatic pressing (Stenhøj 100, Denmark) at 500 MPa. The YSZ pellets were sintered in air at 1350 °C for 6 h with a heating and cooling rate of 120 °C/h. The samples were cleaned by a Triton-100X bath with sonication, rinsed in DI water and immersed in acetone and isopropanol, followed by drying in $N_2$. A negative photoresist (AZ nLOF 2020, Merck, United States of America) was deposited on the YSZ substrates by spin coating (Süss MicroTec Gamma 2M spin coater, Germany). Following the Ni-alloy patterns, the resist was exposed at 160 $mJ/cm^2$ with a maskless aligner (Heidelberg instruments MLA100 Tabletop Maskless Aligner, Germany). The resist was subsequently heat treated at 110 °C for 120 s. The remaining resist pattern was developed for 120 s in a tetramethylammonium hydroxide (TMAH) containing bath. Resist residues were removed from the developed YSZ surface with a (0.8 bar, 100 W) oxygen plasma treatment (Diener Pico Plasma Asher, Germany). The 200 nm Ni-alloy films were deposited by magnetron sputtering (Kurt J. Lesker sputter-system CMS 18, United States of America). For Ni–Cu and Ni–Fe a pressure of 3 mtorr Ar and a power of 150 W (Ni–Cu) or 157 W (Ni–Fe) were used, respectively. The lift-off of the non-exposed resist was performed with a microposit remover 1165 bath (DOW, United States of America).

### 2.2. Model cell electrochemical testing

A three-electrode setup was used to measure the impedance with a potentiostat (Gamry Instruments Reference 600, United States of America) connected to the contact pins inside the model electrode testing stage. The frequency range of 100,000 to 0.2 Hz with ten steps

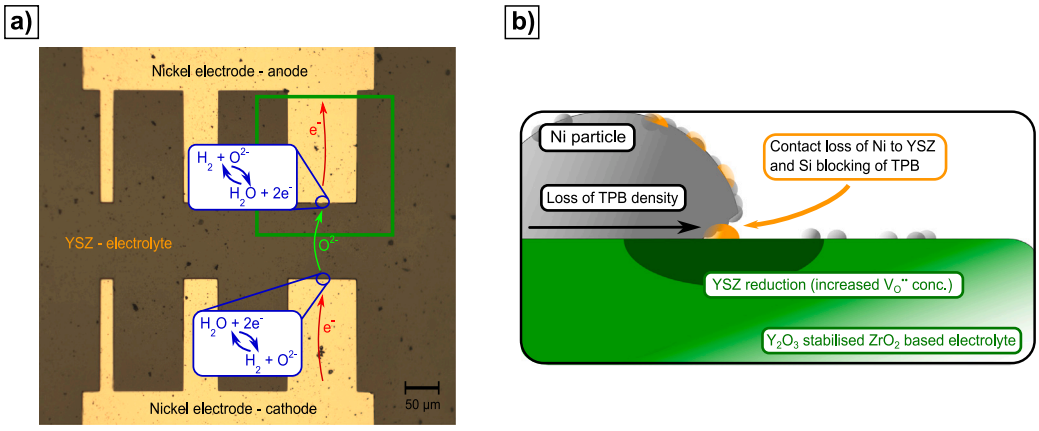



**Fig. 1.** (a) Light microscopy image of the as-prepared alloy films as model electrodes. The LEIS analysis area is marked by the green square. (b) A sketch of the typical degradation of the Ni/YSZ electrodes in contact loss between particles and impurity enrichment at a Ni/YSZ composite electrode.

per decade was measured with an excitation amplitude of 10 mV. The impedance spectra were recorded continuously in 30 min intervals during the potentiostatic polarisation of the model cells over the 40 h lasting tests.

Electrochemical impedance spectroscopy (EIS) was used to track the degradation of the different Ni-alloy samples. Each sample was tested for 40 h in a 0.4 $H_2O$/0.6 $H_2$ mixture in $N_2$ at 750 °C. The cathodic overpotential was controlled against a reference Ni-alloy film deposited on the same sample, but well enough (more than 1 mm) separated to avoid any interference of the working and counter electrode with the reference potential. Ten times the distance between working and counter electrode is considered far enough to exclude interference of working or counter electrode with the reference. A cathodic overpotential of −300 mV can be considered strongly degrading conditions, since device-scale cells are usually exposed to overpotentials > −200 mV at the start of a durability test [8]. This was chosen to show, in accelerated tests, rapid degradation or stability of an electrode without the need of operating for hundreds of hours.

### 2.3. Atomic force microscopy

A Dimension Icon-PT (Bruker, United States of America), operated under ambient conditions, was used to obtain the AFM images. The images were recorded in noncontact tapping mode, using an aluminium-coated monolithic silicon cantilever (Tap150Al probe, BudgetSensors, Bulgaria). The cantilever has a nominal force constant of 5 N/m.

### 2.4. Low energy ion scattering

A Qtac100 (ION-TOF GmbH, Germany), with perpendicular incidence of primary ions, was used to measure the LEIS spectra. The yield of the backscattered ions was recorded at a scattering angle of 145°. To analyse the alloy surfaces, both $He^+$ and $Ne^+$ projectiles were used with an energy of 3 keV and 5 keV, respectively. At each electrode, an area of 200 × 200 µm$^2$ was analysed (marked in Fig. 1 (a)). $He^+$ was used for the lighter impurity elements (e.g., Si) and $Ne^+$ to separate the respective Ni, Fe and Cu peaks. To minimise any beam induced changes in the surface composition, the measurement procedure was kept the same for each alloy sample. An analysis with the $He^+$ beam was always followed by measurements with the $Ne^+$ beam. Calibration of the noble gas beam is performed on the sample holder and only after achieving a stable and reproducible beam are measurements executed on the samples. The background signal in LEIS spectra was not considered for the analysis of integrated peak areas of the different elements.

### 2.5. X-ray photoelectron spectroscopy

The XPS spectra were measured with a K-Alpha+ spectrometer (Thermo Fisher Scientific, United States of America). The instrument was operated at 2x10$^{-9}$ mbar base pressure and is equipped with a monochromated Al K$\alpha$ radiation source (h$\nu$ = 1486.6 eV) . The X-ray spot size was kept at 0.02 mm$^2$ for each electrode. The survey and core level spectra were obtained at a pass energy of 200 eV and 35 eV. A binding energy calibration was performed according to the C 1s peak of adventitious hydrocarbons at 284.8 eV. The Avantage software (Thermo Fisher Scientific, United States of America) was used to analyse the spectra. The peak intensity of all the spectra is normalised against the maximum intensity of the whole binding energy range for each specific electrode and material composition.

### 2.6. DFT calculations

The alloy formation energy, substitutional energy of Si in the alloys and $ZrO_2$ oxygen vacancy ($V_O^{\cdot\cdot}$)-metal interaction were calculated using the GPAW software [25] based on the projector-augmented wave (PAW) method [26] and the atomic simulation environment (ASE) [27]. All calculations were undertaken with a plane-wave basis-set [28]. The RPBE exchange correlation functional [29] was used in all cases. A plane wave cut-off of 600 eV was chosen with a 12 × 12 × 12 k-point grid for the alloy calculations. The $ZrO_2$ surface calculations were performed with a 4 × 4 × 1 k-point grid and a cut-off of 600 eV. The atomic positions in the alloy and $ZrO_2$ systems were relaxed until the forces reached less than 0.03 eV/Å. An initial magnetic moment of 1 $\mu_B$ was used for Ni, Co and Fe.

The alloy formation energy is calculated according to $E_{alloy} = E_{AB} - xE_A - yE_B$, where $E_{AB}$ is the energy of the binary alloy and $E_A$ and $E_B$ are the energies of a single bulk metal atom (then multiplied according to the number of atoms $x$ and $y$ in the alloy). The energies for the metal atoms are calculated from the fcc (Ni, Cu) and bcc (Fe, V, Mn, Co) bulk structures.

The substitutional energy of a Si atom for a Ni atom in the alloys and pure Ni is defined as $E_{Si,sub} = E_{alloy,Si} - E_{alloy} - E_{Si,bulk} + E_{Ni,bulk}$. This formulation uses the calculated energies of the alloy with Si substituted for Ni ($E_{alloy,Si}$) and the energy of the alloy without Si ($E_{alloy}$). The energies of the Ni and Si atoms are calculated based on the energies of a Ni atom in fcc bulk structure ($E_{Ni,bulk}$), and Si atom in $Fd\bar{3}m$ bulk structure for $E_{Si,bulk}$.

The adsorption energy for placing the metal atom at an $V_O^{\cdot\cdot}$ site or preferred site on the surface of the (111) cubic $ZrO_2$ surface slab follows from $E_{Me,vac} = E_{ZrO_2+Me} - E_{ZrO_2,vac} - E_{Me,atom}$. This considers the energy of $ZrO_2$ with metal element in the vacancy ($E_{ZrO_2+Me}$), the energy of cubic $ZrO_2$ with one vacancy ($E_{ZrO_2,vac}$), the energy of

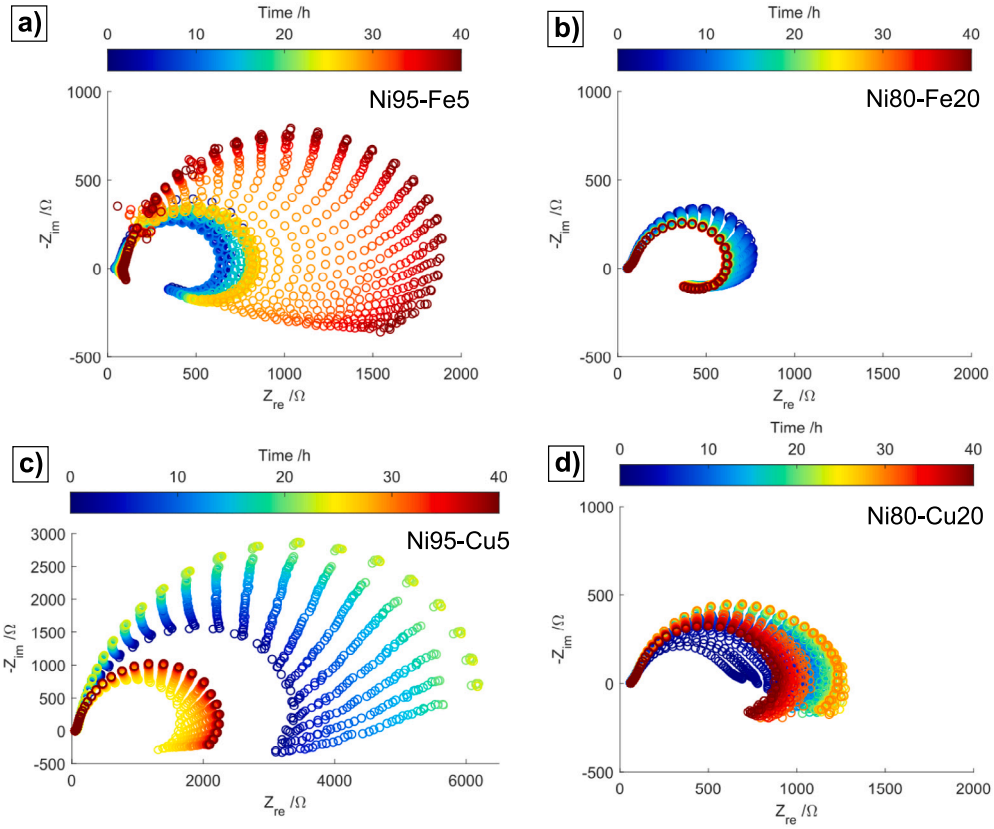



**Fig. 2.** Impedance spectra for each alloy composition are shown in Nyquist plots and were periodically recorded over the 40 h testing period. The subfigures are arranged according to alloy compositions of (a) 95 wt% Ni - 5 wt% Fe, (b) 80 wt% Ni - 20 wt% Fe, (c) 95 wt% Ni - 5 wt% Cu and (d) 80 wt% Ni - 20 wt% Cu. Note that the Ni95-Cu5 electrode in (c) was operated with lower $pH_2O$ for the first 23 h and the Rp is therefore enhanced compared to the results in (a), (b) and (d). A more detailed explanation is given in the manuscript text.

the bulk metal atom ($E_{Me,atom}$). The adsorption energies are, therefore, relative to the bulk structure of the pure metal. The favoured adsorption position on the stoichiometric $ZrO_2$ is in between a Zr and O at the surface and an O at the subsurface layer (in agreement with previous studies [30]). In the case of adsorption near a $V_O^{\cdot\cdot}$ at the surface, the preferred position becomes centred at the vacancy. All surface calculations were performed with 20 Å vacuum perpendicular to the slab. The seven lower atomic rows of the $ZrO_2$ slab were fixed, with the upper 5 (out of 4 $ZrO_2$ layers) allowed to relax as in Ref. [30] for Ni adsorption on $ZrO_2$. The charge of each adsorbed metal atom on the $ZrO_2$ surface was investigated with a Bader charge analysis via the available code from the Henkelman group [31].

Visualisations of the atomic structures can be found in the Supplementary Information.

## 3. Results and discussion

### 3.1. Ni-alloy durability

The evolution of the impedance over the 40 h is shown in Fig. 2 as Nyquist plots for (a) 95 wt% Ni/5 wt% Fe (Ni95-Fe5), (b) 80 wt% Ni/20 wt% Fe (Ni80-Fe20), (c) 95 wt% Ni/5 wt% Cu (Ni95-Cu5) and (d) 80 wt% Ni/20 wt% Cu (Ni80-Cu20), respectively. The degradation is observed as the expanding impedance arcs over time. What becomes apparent from Fig. 2 is the different durability between the ratios of Ni to the alloying metal and Fe or Cu as the alloying element. Ni95-Fe5 in Fig. 2 (a) shows rapid degradation, with an increase in area specific resistance (ASR), as combination of polarisation resistance (Rp) and ohmic resistance (Rs), of 798 Ω to 1885 Ω in 40 h. In contrast, the ratio of Ni80-Fe20 in Fig. 2 (b) activates over the same time span, starting from a similar initial ASR (766 Ω) but decreases to 623 Ω. A similar trend emerges between Ni95-Cu5 in Fig. 2 (c) and Ni80-Cu20 in Fig. 2 (d), with a more rapid degradation of the sample with lower Cu content and better stability and activation of the ASR after 30 h testing for Ni80-Cu20. The Ni95-Cu5 ratio was operated at a lower $H_2O$ content for the first 20 h due to $H_2O$ feed malfunction, resulting in the larger impedance arc at −300 mV. This was corrected during the test and the ASR returned to a lower value (comparable with Ni95-Fe5) during the continued degradation.

**Table 1**
The Rs and Rp values at the beginning of durability tests are listed. Both initial values of operation in low (0–23 h) and high $H_2O$ content (23–40 h) are included for Ni95-Cu5 (high $pH_2O$ in brackets).

| | Ni95-Fe5 | Ni95-Cu5 | Ni80-Fe20 | Ni80-Cu20 |
|---|---|---|---|---|
| Rs /Ω | 41 | 53 (49) | 54 | 58 |
| Rp /Ω | 757 | 3329 (1599) | 712 | 705 |

An important observation is the similar initial ASR between all the samples in Fig. 2 (a), (b) and (d), despite the different alloys and alloy ratios. This agreement can also be found when comparing the initial ASR with an electrode of pure Ni with an ASR of 704 Ω.

To compare changes over time in a more systematic way, the evolution of the Rs and Rp of the impedance spectra is shown in Fig. 3. The initial values used for the normalisation in Fig. 3 are listed in Table 1. Linear degradation rates are assumed in the following. Ni95-Fe5 is the only electrode, which shows an increase in Rs over the 40 h (Rs degradation rate 0–10 h: 1.4%/h, 10–27 h: 3.5%/h and 27–40 h: 1.2%/h). The remaining samples possess a steady Rs throughout the tests (see Fig. 3 (a)). Regarding the Rp evolution, it is noteworthy

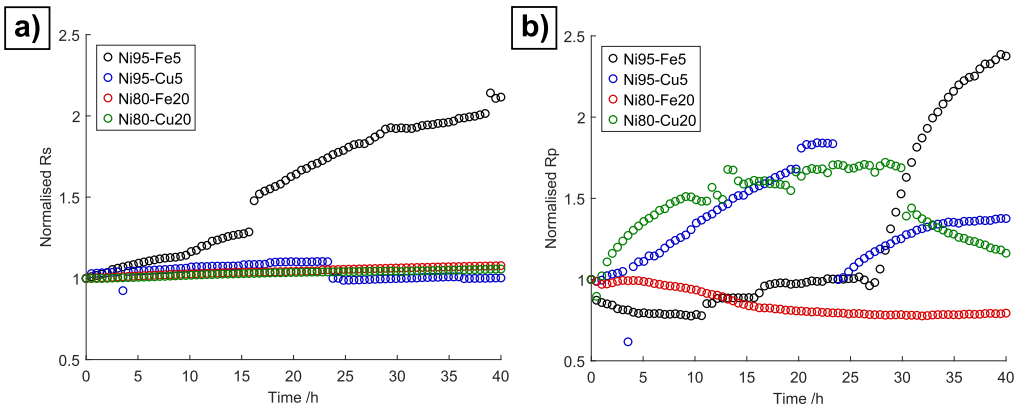



**Fig. 3.** (a) The ohmic resistance (Rs) evolution of the different alloy compositions is shown according to the spectra presented in Fig. 2. (b) The evolution of the polarisation resistance (Rp) is depicted according to the spectra in Fig. 2.

that the Fe containing alloys initially show activation, whereas the Cu alloyed electrodes depict degradation from the onset of a test. The Rp of Ni95-Cu5 then stabilises towards the end of the test after two phases of degradation in low $pH_2O$ (Rp rate: 3.6%/h) and high $pH_2O$ (2.9%/h). In contrast, Ni80-Cu20 shows activation of the Rp after 30 h of operation (−3,2%/h), while reaching a plateau over the initial 30 h of degradation (2.3%/h). The Rp of Ni80-Fe20 activates initially (rate from 0–20 h: −1.0%/h) and then stabilises. The Rp of Ni95-Fe5 reveals a slight activation initially, then a modest degradation and after 27 h an accelerated degradation. Here the trends follow the Rs degradation: (1) 0–10 h: activation of Rp (−2.2%/h) and slow degradation of Rs (1.4%/h), (2) 10–27 h: modest degradation of Rp (1.4%/h) and fast degradation of Rs (3.5%/h) and (3) 27–40 h: rapid degradation of Rp (10.9%/h) and slowed down Rs degradation (1.2%/h). These rates indicate a correlation of the fast degradation of Rs from 10–27 h with the rapid Rp degradation after 27 h. A percolation loss of Ni95-Fe5 particles or alloy film could here initiate an increase in Rp when the density of active triple phase boundary (TPB) decreases due to a critical percolation loss deactivating parts of the alloy network.

To assess if the different gas phase concentrations of $H_2O$ have introduced deviating degradation rates for Ni95-Cu5, the Rp changes in low $pH_2O$ (3.6%/h) and high $pH_2O$ (2.9%/h) can be compared. These rates show that the electrode degraded comparably in both $pH_2O$ regimes without seemingly accelerated degradation during the low $pH_2O$ operation. This indicates that the operation did not induce accelerated degradation nor cause degradation otherwise not observable. Nonetheless, the two different $pH_2O$ regimes are noteworthy and should be considered when comparing the results between Ni95-Cu5 and the other alloy compositions.

The comparable Rp and Rs between alloys (see Table 1) confirm the control over the deposition of the alloy electrodes in terms of TPB and interfacial area. Similar alloy film density and thickness can also be expected from the similar deposition parameters (see Section 2.1). Since surface adsorption and diffusion would likely differ between alloy compositions, EIS measured performance should deviate between the alloy compositions if these would be limiting. This is not the case for the conditions considered here and shows that such effects play a secondary role. The different proportions between TPB to interface area for model compared to porous electrodes could possibly introduce additional interface reactions contributing to the measured EIS, as discussed by Doppler et al. [32,33]. Therefore, the electrochemical performance measurements are not fully transferable and comparable to porous composite electrodes.

### 3.2. Ni-alloy morphology changes

To assess the Ni-alloy electrodes after each durability test, atomic force microscopy is utilised due to its nanometre resolution and it not requiring destructive sample preparation. Images of the reference alloy films, kept under the same conditions on the same sample, are used to maximise comparability between observed changes in film morphology.

In general, the morphologies of the anode and reference alloy films show high similarity after the tests. It is noteworthy that the Ni95-Fe5 electrodes break apart into a partly percolating network of alloy particles under cathodic bias, anodic bias and at the reference electrode in Fig. 4 (a), (b), and (c). This could be explained by the instability of Ni–Fe alloys in highly Ni rich conditions, as reported in Ref. [34]. Such coarsening is not observed for the other alloy electrodes, where the alloy remains percolating on the surface of the zirconia. What differs between cathode and anode/reference is the coverage of the YSZ surface with a higher density of nanoparticles, indicative of cathodic-induced mobility of the Ni95-Fe5 alloy film.

The Ni80-Fe20 electrodes show only minor film restructuring. Nanoparticles on the YSZ surface can be observed in all cases (cathode, anode, and reference) but the dispersion of the nanoparticles reveals subtle differences. The anode in Fig. 4 (e) and reference in (f) shows a clustering of nanoparticles around the grain boundaries of YSZ. The grain boundaries of YSZ present structurally more defective regions of the surface [35], where nanoparticles could accumulate. Contrarily, the YSZ surface at the cathode shows larger nanoparticles, which are more evenly distributed, independent of the grain boundaries of YSZ. This suggests an accumulation of alloy nanoparticles around defect-rich regions (grain boundaries) at the anode and reference (marked by blue arrows in Fig. 4), when the YSZ surface is kept at equilibrium with the gas phase or under even more oxidising conditions (anode). In contrast, at the cathode, the reducing conditions (higher $V_O^{\cdot\cdot}$ concentrations) on the YSZ surface around the TPB result in dispersion and mobility of the alloy nanoparticles. Such trends were previously observed for metal/oxide catalyst systems [36,37] as well as metal exsolution perovskites [38].

The lower mobility of the Ni–Cu alloys is generally observed, and the films exhibit higher connectivity with less nanoparticle formation, independent of the polarisation. However, at several locations at the TPB (marked by red arrows in Fig. 4 (g) and (j)), the Ni–Cu alloy film shows contact loss and restructuring away from the TPB under cathodic bias, visible in Fig. 4 (g) and (j). This suggests a lower interface adhesion of the Ni–Cu alloys compared to the Ni–Fe versions, consistent with previous DFT calculations [19].

To provide some quantitative values for the above discussion of AFM results, the root mean square (RMS) roughness values of alloy and YSZ surface are listed in Table 2. The RMS roughness indicates a higher density of larger nanoparticles on the YSZ surface after dispersion of the Ni95-Fe5 film. For the other samples, the RMS roughness is comparable for all YSZ surfaces close to the TPB. This indicates no clear enrichment

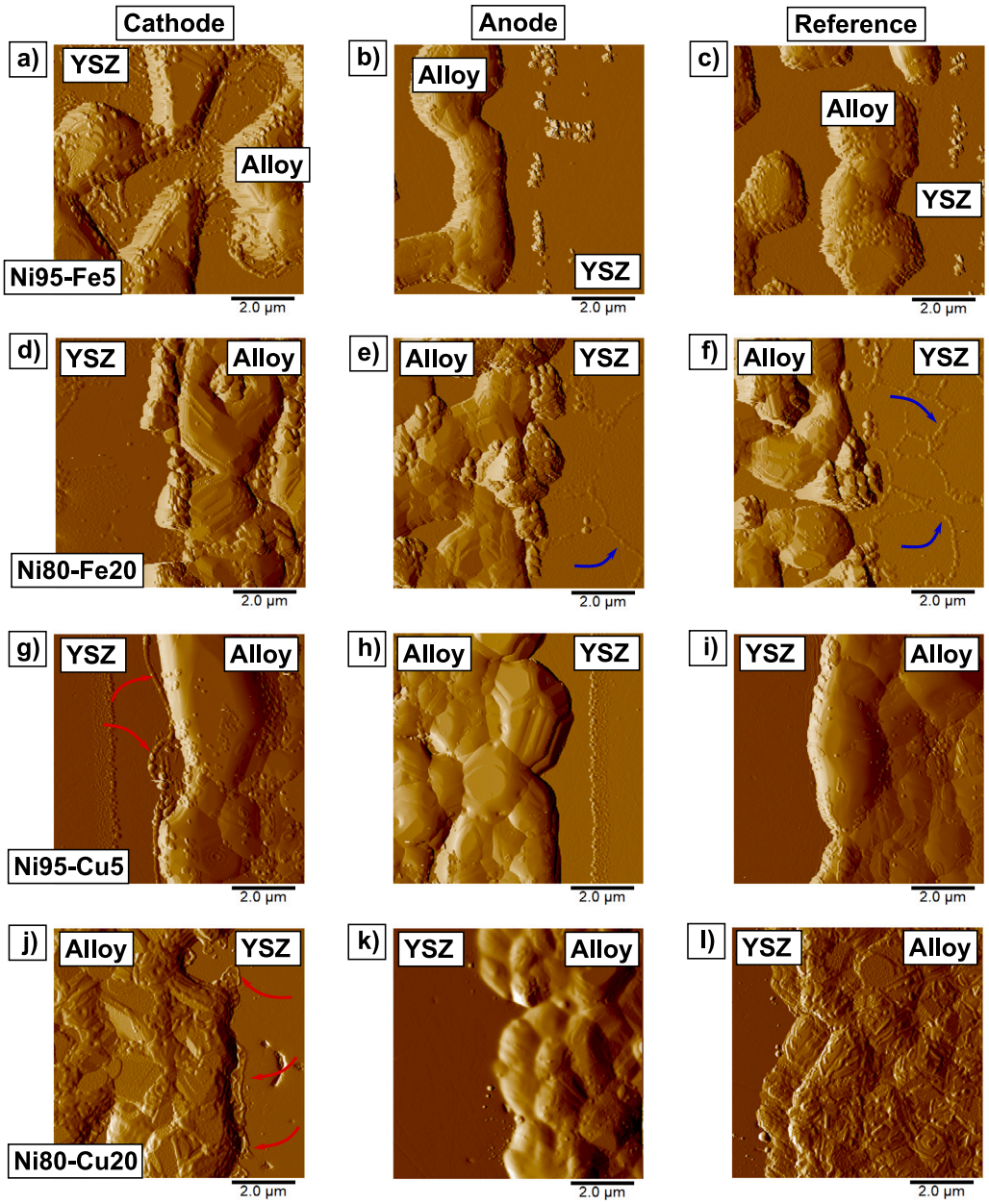



**Fig. 4.** AFM images are depicted for cathode, anode and reference alloy films for the different alloy compositions of Ni95-Fe5 in (a), (b) and (c), Ni80-Fe20 in (d), (e) and (f), Ni95-Cu5 in (g), (h), and (i) and Ni80-Cu20 in (j), (k) and (l). The regions of contact loss of Ni–Cu film and YSZ are marked by red arrows. The nanoparticle accumulation around the YSZ grain boundaries are indicated by blue arrows in (e) and (f). (For interpretation of the references to colour in this figure legend, the reader is referred to the web version of this article.)

**Table 2**
The RMS roughness of the alloy and adjacent YSZ surface is listed for the different alloys and cathode, anode and reference electrode.

| | Cathode - alloy | Cathode - YSZ | Anode - alloy | Anode - YSZ | Reference - alloy | Reference - YSZ |
|---|---|---|---|---|---|---|
| Ni95-Fe5 | 91 nm | 15 nm | 91 nm | 31 nm | 90 nm | 19 nm |
| Ni95-Cu5 | 120 nm | 8 nm | 117 nm | 7 nm | 124 nm | 1 nm |
| Ni80-Fe20 | 170 nm | 7 nm | 158 nm | 8 nm | 206 nm | 9 nm |
| Ni80-Cu20 | 73 nm | 13 nm | 105 nm | 4 nm | 58 nm | 8 nm |

of nanoparticles for any of the intact alloy film electrodes nor according to the polarisation (anode, cathode or reference electrode). The alloy films have generally a high RMS roughness. Again, this is independent of the polarisation and indicates thermal coarsening during operation at 750 °C. Some more subtle differences between the electrodes can be seen in the height distribution of the alloy electrode films, which is presented in the Supplementary Information. It is noteworthy that the dispersed Ni95-Fe5 electrode has the lowest RMS roughness of the alloys. In contrast, the Ni80-Fe20 electrodes show highest RMS roughness, which suggests most extensive morphological changes. The Ni–Cu electrodes depict lower roughness, as is visible in Fig. 4 compared with the Ni80-Fe20 alloy surface. More information and discussion on alloy film height and height distribution after testing is presented in the Supplementary Information.

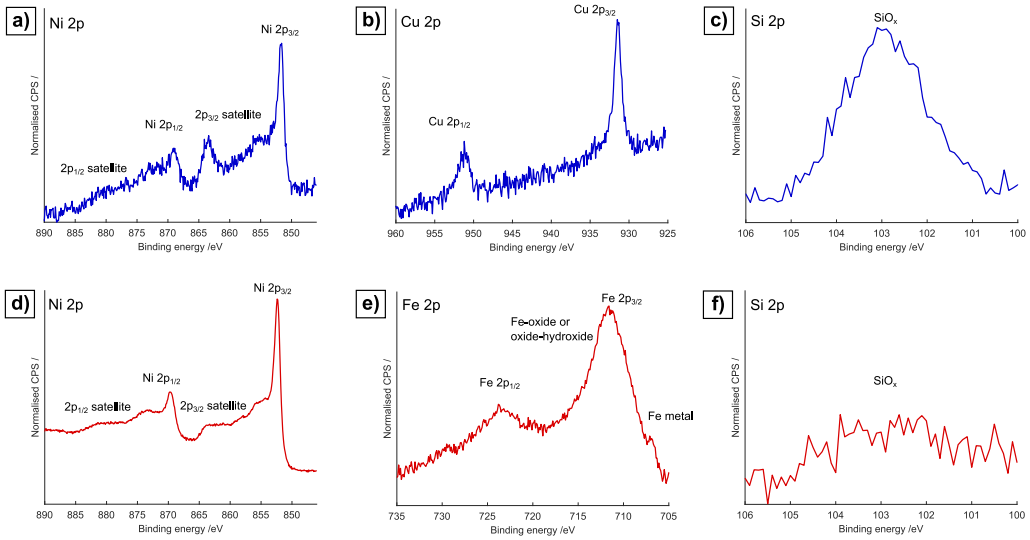



**Fig. 5.** The specific binding energy ranges of Ni 2p, Cu or Fe 2p and Si 2p are shown for the cathode surface of Ni80-Cu20 in (a), (b) and (c) and Ni80-Fe20 in (d), (e) and (f).

In Fig. 4 (b), (c), (g) and (h), a straight line of nanoparticles can be observed. Similar observations have been made for other sputter-deposited Ni electrodes [20,39]. This line is a result of the imperfect photoresist and sputtering deposition. Negative photoresists generally show an undercut of the resist pattern after exposure and development. The resist walls are then not perpendicular to the substrate because of the weaker ultraviolet (UV) light exposure of the lower regions of the resist. These regions are then slightly dissolved in the developer bath resulting in tilted resist side walls. As a consequence, the sputtering can lead to alloy deposited underneath the undercut resist area. When the alloy is not fully incorporated into the main film during heat treatment and operation, leftover nanoparticle can be found on the YSZ substrate. Since the substrate roughness and porosity can locally vary, the effect is at some locations more pronounced than at other parts of the samples. It should further be noted that the Ni95-Cu5 anodic and cathodic polarisation introduces no driving force to attract and transport the non-percolating Ni-alloy nanoparticles towards the polarised TPB, as can be seen in Fig. 4 (g) and (h).

### 3.3. Surface composition after testing

X-ray photoelectron spectroscopy is used to analyse the surface composition found after the tests. The Ni 2p and Fe or Cu 2p regions are shown in Fig. 5 (a), (b), (d) and (e). Si impurities are found, indicated by the Si 2p peak in Fig. 5 (c) and (f), for both Ni80-Cu20 and Ni80-Fe20. Si species are regularly observed as trace impurities in SOECs operated with $H_2O$ fuel gas [12] and raw powders of YSZ are also known to contain Si impurities [14], which segregate to the surface during sintering. The presence of Si impurities at the reference alloy films outlines a possible deposition from the gas phase without polarisation and Si already present in YSZ powders before sample preparation.

Note that the XPS measurements were performed ex-situ and after exposure of the samples to air. The oxidation states of Fe and Si are here not indicative of the surface composition during polarisation and exposure to $H_2/H_2O$ atmospheres. The analysis was performed to confirm the presence of Si on the electrode surfaces for the following analysis with low energy ion scattering. A deconvolution of the Fe 2p region is therefore not presented, since exposure to air could lead to misleading interpretation of the oxidation state during electrochemical testing. A quantitative analysis of elemental ratios is also not performed because of the high noise levels in the XPS data recorded from the small analysis areas of the electrode tip regions.

In order to investigate the Si distributions and possible segregation in the alloy films, low energy ion scattering is used due to its surface sensitivity of a few atomic layers [40]. This advantage and the better focus on the precise location of the alloy electrodes during measurements of micrometre sized areas make the technique compatible to XPS and able to more accurately present the surface composition of the alloys after electrochemical testing.

The LEIS analysis reveals differences between the Si content found on the alloy surfaces after treatment under the same conditions and over the same time frame, as can be seen in Fig. 6 (a) and (b). As a general trend (illustrated in Fig. 6 (e)), the higher the Fe or Cu content in the Ni-alloy, the lower the amount of Si found on the surface. In addition, Ni80-Fe20 shows a lower amount of Si compared to the respective Ni–Cu counterpart. As a reference, the Si content of a pure Ni electrode, without polarisation, is illustrated after 30 h at the same temperature and in the same gas atmosphere. Thus, the Ni80-Fe20 electrodes, independent of polarisation, have only 1/6 of the amount of Si at the surface compared with pure Ni.

Possible effects of surface oxides due to the differences in Cu and Fe termination at the surface are discussed in the Supplementary Information. As a summary, the oxygen peak of the surface follows qualitatively the Si peak. Therefore, the oxygen ratio (O/(Ni/Cu/Fe + Zr/Y)) is lowest for the Ni80-Fe20 electrodes with lowest Si ratio (Si/(Ni/Fe/Cu + Zr/Y)). In addition, the Si and O ratios of Ni95-Fe5 are highest among all electrodes, showing that a large part of the O peak originates from Si at the surface. This indicates that no fully surface-blocking Fe-oxide layer has formed for Ni80-Fe20 or Ni95-Fe5 (even after testing), which could artificially lower the detected Si peak. The electrochemical measurement support this by showing the most durable performance for Ni80-Fe20. A direct connection between electrochemical testing and surface composition will however only be possible with in-situ spectroscopy.

The surface composition of the alloy films is additionally important due the potential role in surface reactivity of the alloys, i.e., adsorption and dissociation of gas-phase molecules. In the case of Ni80-Cu20 shown in Fig. 6 (c), the integrated Cu and Ni peak areas can be compared for anode, cathode and reference. The Ni–Cu films under cathodic, anodic or no bias depict the same ratio between Cu and Ni, as illustrated in Fig. 6 (f). The same can be observed for Ni80-Fe20 under anodic bias or OCV. The ratio deviates under cathodic polarisation, when a 3× higher Fe intensity is detected.

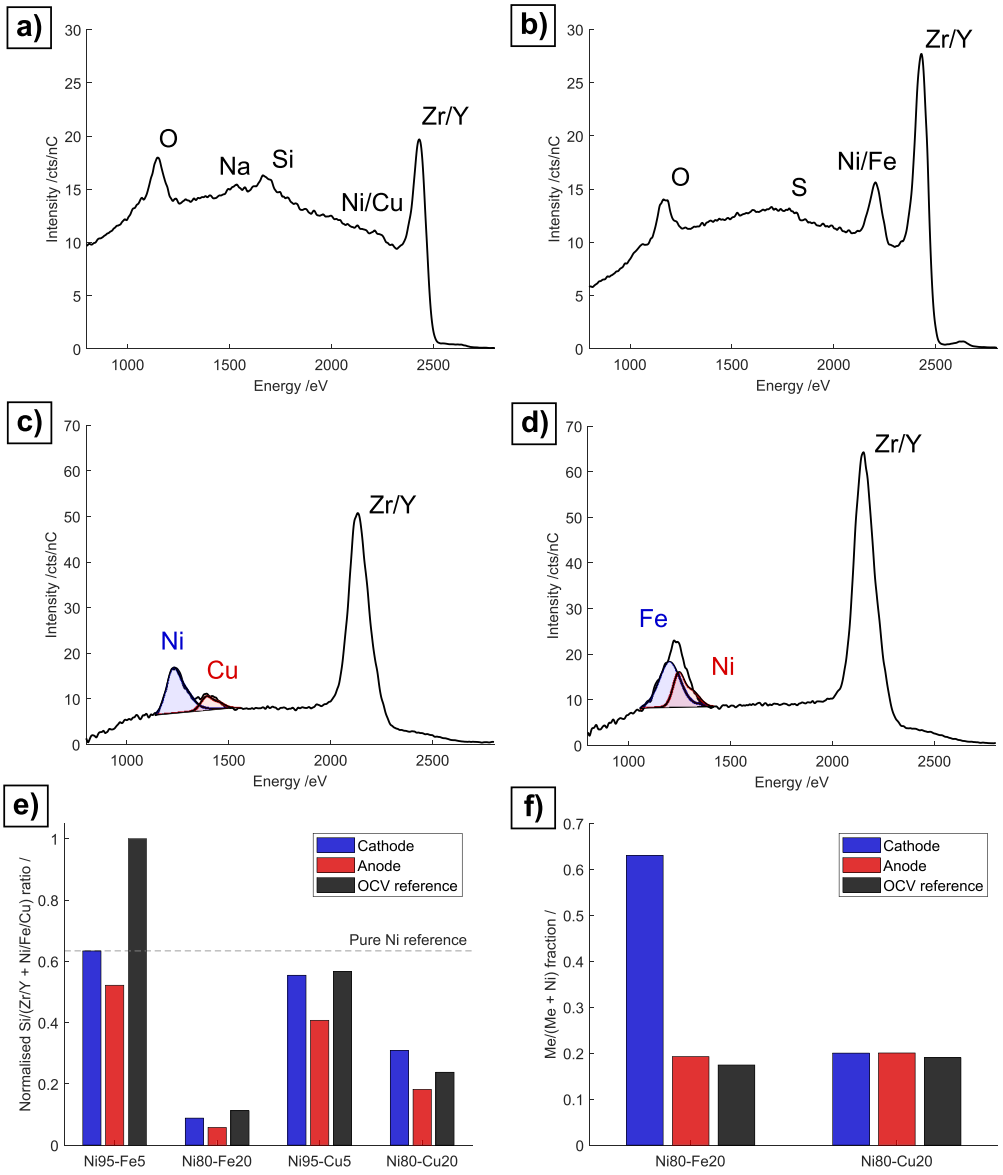



**Fig. 6.** LEIS spectra recorded with $He^+$ are shown for the cathode of (a) Ni80-Cu20 and (b) Ni80-Fe20. It should be noted that heavier elements (e.g., Ni and Cu or Fe) cannot be separated with $He^+$. The same electrode areas analysed with $Ne^+$ are depicted for (c) Ni80-Cu20 and (d) Ni80-Fe20. (e) The ratio of integrated Si peak area per Ni-alloy and Zr/Y peaks (Si/(Zr/Y + Ni-alloy)) is shown for the different compositions. The values are normalised against the value of the reference electrode of Ni95-Fe5. As a reference, the Si amount on a pure Ni electrode is shown, without polarisation, after 30 h in the same gas atmosphere and at same temperature as the alloy samples. (f) The fraction of Fe or Cu on the electrode surface is illustrated as Me (Fe or Cu)/(Me + Ni).

The observations of a stable alloy composition match the expected fcc phase diagrams of Ni–Fe and Ni–Cu alloys in the investigated temperature range [23,24]. The higher surface energy of Fe compared with Ni should also, in an equilibrium state, prevent segregation of Fe [41]. However, for Ni80-Fe20 under cathodic bias, a clear enrichment of Fe towards the top atomic layers of the alloy film can be observed through LEIS, as is shown in Fig. 6 (f).

The observation of Fe enrichment at the Ni80-Fe20 surface leads to a stable film (no delamination as for Ni–Cu) and significantly reduced Si uptake, which indicates the protective properties of the alloys against degradation. Transport of Fe to the surface and TPB could potentially prevent splitting of the alloy film into separated particles (as observed for Ni95-Fe5). It further implies prevention of continued Si uptake, as indicated by the clearly reduced Si content for the larger amount of Fe in the Ni–Fe alloys. Ultimately, this enrichment of Fe to the surface and TPB of the electrode protects and even activates the performance compared to that of the other alloys. These trends can be understood as self-protecting properties of favourable restructuring of the metal phase (Ni–Fe) in the electrode instead of the generally (for pure Ni) reported negatively affecting and degrading restructuring.

In addition, a clearly lowered Si ratio can be observed for all Ni-alloy electrodes after treatment under anodic bias. An electrochemical deposition of Si at the electrode surface was previously suggested under cathodic bias [8,12,42]. An equal or higher intensity of Si is also detected here for the Ni–Cu electrodes after cathodic bias compared with the reference electrodes. The Ni–Fe cathodes show lower Si intensity compared to the reference electrodes further indicating protective properties of the electrode due to Fe segregation to the surface. The removal (at anode) and deposition (at cathode) of Si could generally follow from $Si(OH)_4 + 4\,e^- \rightleftharpoons SiO_2 + 2\,H_2 + 2\,O^{2-}$. This is a hypothesis based on correlations observed for all samples after anodic bias, when less Si is detected compared to cathodes and reference electrodes. Independent

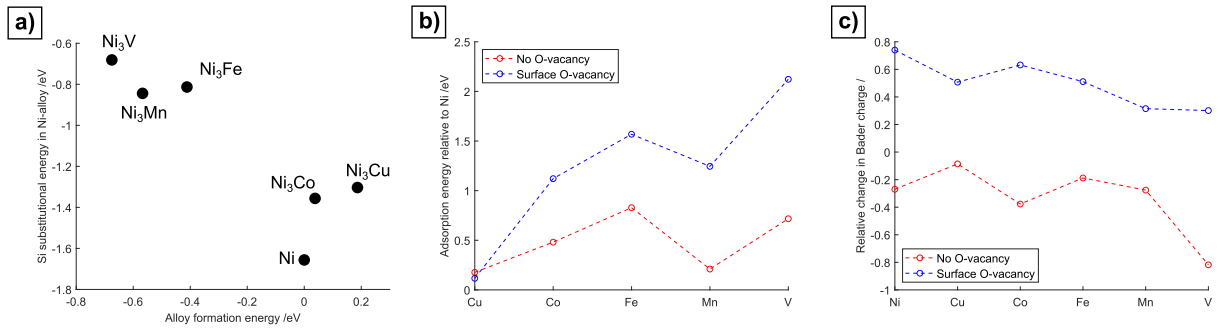



**Fig. 7.** (a) The substitutional energies of Si in $Ni_3Me$ are shown for replacing Ni with Si (y-axis) and the alloy formation energy of the different alloys ($Ni_3Me$) is plotted along the x-axis. More information on the definition of energies and equations to calculate them is given in Section 2.6. (b) The adsorption energy for the transition metals (Co, Cu, Fe, V, or Mn) at an oxygen vacancy or favoured adsorption site without vacancy is depicted relative to Ni adsorbed at the same location on a (111) cubic $ZrO_2$ surface. (c) The relative change in Bader charge of the adsorbed metal atom is compared for a surface oxygen vacancy and stoichiometric $ZrO_2$ surface site.

of the alloy composition removal of Si is observed at the anodes after tesiting in Fig. 6 (e). These observations deserve future work to further establish the relations for Si behaviour under different bias.

### 3.4. Underlying processes

The durability of Ni80-Fe20 and Ni80-Cu20 raises questions about the fundamental processes at play and how these could be translated to other binary Ni-alloys. In such context, density functional theory is commonly used to establish an atomic scale understanding of the underlying principles, despite not fully representing the conditions nor structure of the electrodes experimentally investigated. Moreover, once experimental trends and properties can be reproduced, DFT offers opportunities for screening other (not experimentally characterised) alloy compositions. This should ideally outline binary alloys worth researching in future studies.

The alloy formation energy is used as indicator for the formation of a single alloy phase of the composition $Ni_3Me$. The substitutional energy of a Si atom for a Ni atom in pure fcc Ni or fcc $Ni_3Me$ alloy (Me representing Fe, Cu, Mn, V, or Co) is applied to indicate the favourability of Si dissolution in the alloy. A lower energy would suggest a preferred uptake of Si in the transition metal system (considering the elevated temperatures during the experiments). All the reference energies of the atoms are calculated from the preferred bulk structures. The equations and definitions of the energies can be found in Section 2.6. The atomic structures are visualised in the Supplementary Information.

The results for Si substitution to Ni or $Ni_3Me$ can be found in Fig. 7 (a). The Si substitutional energy for replacing one Ni atom with Si is lowest in the pure Ni case, supporting reports of the accumulation of Si impurities on Ni particles and dissolution under reducing (reduction of $SiO_x$ to Si) conditions in SOECs [43]. The Si substitutional energy is increased for the addition of Cu and Fe to Ni, resulting in a more positive energy difference for substituting Si for Ni. This could translate into fewer interactions of Si with Ni–Fe and Ni–Cu alloys compared to pure Ni, as also experimentally found by varying the amount of alloy elements (Fig. 6). Adding Cu restricts the amount of Si (see Fig. 6 (e)). The effect is enhanced for Fe, which also experimentally shows fewest Si at the surface. Those observations agree with the amount of Si detected by LEIS at the surface of the Ni–Fe and Ni–Cu alloys, decreasing with increasing content of Fe and Cu.

It is important to note that Si interaction (through the substitutional energy) with the alloys is only analysed on the basis of a bulk alloy system. This is done to establish trends before attempting to reproduce the complex structure of the TPB and surface regions with a broader experimental understanding of the atomic structure in the future. Further, diffusion of impurities, grain boundary effects and interfacial phenomena of the Ni-alloy/YSZ electrodes are not considered in the DFT calculations but might crucially contribute to impurity accumulation and transport.

To further analyse alloy-effects on Si substitution and if they could be found for other Ni-alloys, other binary alloy compositions are investigated, consisting of Co, Mn and V. The possible alloy stability can be identified, using the alloy formation energy and substitutional energy of Si in a potential alloy as screening parameter. For this, we expanded the list of binary Ni-alloys to $Ni_3Co$, $Ni_3Mn$ and $Ni_3V$. The results of the alloy formation energy are plotted in Fig. 7 (a), placing $Ni_3Fe$ in the upper left corner, indicative of a single phase Ni-alloy with possible restrictions on Si uptake due to the increased substitutional energy (compared with pure Ni). The same properties can be achieved by alloying with Mn and V, suggesting a similar behaviour to Fe. A more negative alloy formation energy (more stable Ni-alloy) can be seen as an indicator for a higher barrier of Si uptake in the alloy.

To give indications on how Fe can enrich to such an extent at the surface of the Ni80-Fe20 alloy under cathodic experimental conditions, the interactions of Ni, Fe and Cu (and other transition metals) with a reduced and stoichiometric (111) surface of cubic $ZrO_2$ are investigated. In order to compare trends holistically, the metal atom is either placed on an $V_O^{\cdot\cdot}$ (to mimic reducing conditions at the YSZ interface) or the preferred stoichiometric $ZrO_2$ adsorption site. This is considered a cleaner model system to represent the more complex cubic YSZ or TPB. In addition, the energies in Fig. 7 (b) are relative to the adsorption of Ni since differences with Ni (explaining observed transport of alloyed elements) are of interest and not absolute adsorption energies. In an equilibrium case, Fe is not expected to segregate, exemplified by the negative alloying energy and a higher surface energy of pure Fe over pure Ni, which would indicate no Fe segregation [41]. Since it is found experimentally that Fe enriches only at the cathodically polarised surface, a correlation exists between the reducing conditions at the alloy/YSZ interface and the Fe enrichment.

The DFT adsorption results are shown in Fig. 7 (b) and indicate less favourable interactions of Fe with the vacancy than for Ni. The difference in adsorption energy is also elevated for Fe in an oxygen vacancy site than on the stoichiometric $ZrO_2$ surface. It can be understood as Ni interacting preferably with the reduced $ZrO_2$/YSZ (0.74 eV lower adsorption energy) compared to Fe when the electrode is cathodically polarised. Contrarily, the energies for Cu follow the adsorption energy trends of Ni. The adsorption energy at a $V_O^{\cdot\cdot}$ site increases relative to Ni according to Co < Mn < Fe < V, as shown in Fig. 7 (b) (deviating even stronger than compared to the stoichiometric surface).

An analysis of the relative change in Bader charge can elucidate the findings by indicating a positive charge of the metal atom (ionic bond) on the stoichiometric (near $O_O^{\times}$) adsorption site, as is show in Fig. 7 (c).

In contrast, the metal atom is charged negatively when adsorbed right next to a vacancy site, which results in an interaction with the trapped electrons at the vacancy (following $2Zr_{Zr}^{\times} + O_O^{\times} \longrightarrow 2Zr_{Zr}^{'} + V_O^{\cdot\cdot} + \frac{1}{2}O_2$ or the formation of a defect-rich electrochemical double layer at the Ni/YSZ interface under cathodic bias). The results show that in all cases some charge is gained by the metal atom at the vacancy. However, the energetic cost is influenced by the electron affinity of the metal itself. Transition metals with high electron affinity, like Ni and Cu, possess a lower and similar adsorption energy, whereas Co, Fe, Mn and V show increasing adsorption energies following the lowered electron affinity (trends in electron affinity can be found in Ref. [44]).

The opposing interactions of low (Mn, Fe, V) and high electron affinity metals (Ni,Cu) with partly reduced YSZ can hence lead to surface regions enriched in the low affinity alloy element. A possible explanations could here be the high electron affinity metal (Ni) moving towards reduced interfaces (under cathodic bias) leaving a low affinity metal (i.e., Fe-enriched) surface. Alternatively, the low electron affinity element could segregate to the surface, being repelled from the reducing conditions at the interface. The segregation behaviour of Fe for a Zr or O terminated interface was suggested by Malyi et al. through DFT calculations [19], indicating that Fe would preferentially segregate from Zr-terminated interfaces (similar to $V_O^{\cdot\cdot}$ rich interfaces under cathodic polarisation). Both scenarios deserve further research on the fundamental transport processes responsible. What is observed here is that the combination of low and high electron affinity metal in an alloy can offer self-protecting properties due to the different interactions with YSZ under reducing conditions, supported by the DFT results. These opposite interactions under cathodic bias can be understood as a possible driving force behind the apparent transport.

The findings of Ni–Fe, Ni–V and Ni–Mn as possibly more durable electrodes agree with the experimental observations of improved adhesion to YSZ for Ni–Fe and Ni–Mn in Ref. [20]. This can be further based on Fe, V and Mn being more oxophilic than Ni and Cu [45], leading to stronger interface adhesion (as also shown by DFT in Ref. [19]). Therefore, the Ni–Cu electrodes show similar behaviour to pure Ni at the interface with YSZ (as already shown for pure Ni in Ref. [46]). Oppositely, the Ni–Fe are stabilised at the TPB with Fe enrichment and better interface adhesion (matching the stability of our and related experimental findings [20]).

Since Fe less favourably interacts with oxygen vacancies and increases the energy for Si uptake, Fe-rich layers can act to protect against Si deposition and degradation of the alloy/YSZ interface. Both follow from the durability of Ni80-Fe20 with significantly lowered Si amounts on the surface and no delamination of the electrode film. The proposed less favoured uptake of Si by Fe enrichment at TPB and surface matches the activation of the impedance, as was observed experimentally in the first 20 h (see Section 3.1). The results suggest that the proposed self-protecting properties of a Ni-alloy can be achieved with Ni–Fe. The conditions under which electrodes with pure Ni usually degrade by Ni/YSZ contact loss (below −200 mV [8]), can be impeded by the formation of Fe enriched regions under strong cathodic potentials. The self-protecting Fe transport under high overpotential thus suppresses the degradation, otherwise observed in the contact loss to YSZ and impurity accumulation. The removal of Si impurities can here lead to less degrading conditions at the TPB (lower resistance associated with $O_O^{\times}$ insertion).

In general, Ni-alloys placed in the upper left corner of Fig. 7 (a) and with less favourable energy of interaction with a $V_O^{\cdot\cdot}$ (Fig. 7 (b)) are promising alloys with possible self-protective properties in SOEC fuel electrodes. Any enrichment of alloy elements, which similar to Fe limit the accumulation of Si at the electrode surface and the delamination of the metal phase from YSZ, could offer intrinsic self-protecting properties. In particular, since the formation of the protective layer is correlated with the cathodic bias, the degradation usually driven via the same overpotential can be prevented, as was shown with Ni–Fe in this study under extreme cathodic polarisation (−300 mV).

The high overpotentials make the results despite the 40 h testing times comparable to degradation of porous electrodes, which show rapid onset of degradation below overpotentials of −100 mV [8,47]. Since gas phase impurity effects are known to mostly degrade the reaction paths at the TPB (even for model electrodes with higher interfacial areas [33]) the protection properties of Fe against Si impurities are expected to be transferable to porous electrodes. Any microstructural degradation rates are expected to differ between porous and model electrodes. Therefore, possible protective effects against microstructural degradation will require testing of alloy electrodes in porous electrode settings. Tests on device SOEC-scale can further establish processing of the electrodes and implementation in full SOEC structures. Such considerations are highly relevant to transfer the fundamental findings of this work to the device-scale.

## 4. Conclusions

In conclusion, binary Ni-alloys are investigated in this work as potentially more durable alternatives to pure Ni in solid oxide electrolysis cells. Based on the experimental characterisation of Ni–Fe and Ni–Cu alloys in model electrode systems, the sought after durability is found for Ni–Fe because of the restriction of Si uptake due to alloying and better alloy/YSZ adhesion. The properties are assigned to the favourable restructuring of Fe in the Ni–Fe system under cathodic bias. The results indicate that this restructuring is initiated by the reduction of YSZ at the alloy/YSZ interface under cathodic bias, which also causes formation of a protective Fe-rich alloy surface. The Fe layer is found to decrease the extent of Si uptake and Ni/YSZ contact loss, two processes that cause considerable degradation in the pure Ni/YSZ electrodes in SOEC mode. In contrast for a Ni–Fe cathode, activation of electrochemical performance is observed under high cathodic polarisation (−300 mV).

The experimental findings are supported on a fundamental level by DFT calculations, showing trends in terms of the alloy formation energy, $ZrO_2$ oxygen vacancy-metal (Ni and alloyed metals) interaction, and substitutional energies of Si in the alloys. A synergy of all three properties in an increased energy barrier for the dissolution of Si and a higher barrier for interactions between alloyed metal and vacancy was found for different binary alloys (Ni–Fe, Ni–V, and Ni–Mn). These findings outline alloys that could show self-protecting properties, as it was observed experimentally for Ni–Fe. Alloys with properties similar to Ni–Fe, Ni–V, and Ni–Mn should hence be considered in possible self-protecting fuel electrode composites for SOECs.

## CRediT authorship contribution statement

**Julian Taubmann:** Writing – review & editing, Writing – original draft, Visualization, Software, Methodology, Investigation, Conceptualization. **Henrik H. Kristoffersen:** Writing – review & editing, Supervision, Investigation. **Christodoulos Chatzichristodoulou:** Writing – review & editing, Supervision. **Jan Rossmeisl:** Writing – review & editing, Resources. **Stephen J. Skinner:** Writing – review & editing, Supervision, Resources. **Henrik Lund Frandsen:** Writing – review & editing, Supervision, Resources, Project administration, Funding acquisition, Conceptualization.

## Declaration of competing interest

The authors declare that they have no known competing financial interests or personal relationships that could have appeared to influence the work reported in this paper.

## Acknowledgements

The presented work has received funding from the Innovation Fund Denmark - 1150-00001B. The DFT computations received support from the Novo Nordisk Foundation Data Science Research Infrastructure 2022, Denmark Grant with no. NNF22OC0078009. S. J. S. acknowledges the support from the Royal Academy of Engineering for a Research Chair, United Kingdom (RCSRF/1243-2021).

## Appendix A. Supplementary data

Supplementary material related to this article can be found online at https://doi.org/10.1016/j.jpowsour.2025.238678.

## Data availability

Data for this article, including relaxed DFT structures, spectroscopic (LEIS, XPS) and EIS raw data, are available at DTU data repository https://doi.org/10.11583/DTU.29086796.v1.

## References


[1] O.J. Guerra, J. Eichman, J. Kurtz, B.-M. Hodge, Cost competitiveness of electrolytic hydrogen, Joule 3 (10) (2019) 2425–2443.

[2] T. Capurso, M. Stefanizzi, M. Torresi, S. Camporeale, Perspective of the role of hydrogen in the 21st century energy transition, Energy Convers. Manage. 251 (2022) 114898.

[3] D. Tonelli, L. Rosa, P. Gabrielli, K. Caldeira, A. Parente, F. Contino, Global land and water limits to electrolytic hydrogen production using wind and solar resources, Nat. Commun. 14 (1) (2023) 5532.

[4] A. Hauch, R. Küngas, P. Blennow, A.B. Hansen, J.B. Hansen, B.V. Mathiesen, M.B. Mogensen, Recent advances in solid oxide cell technology for electrolysis, Science 370 (6513) (2020) eaba6118.

[5] H. Nami, O.B. Rizvandi, C. Chatzichristodoulou, P.V. Hendriksen, H.L. Frandsen, Techno-economic analysis of current and emerging electrolysis technologies for green hydrogen production, Energy Convers. Manage. 269 (2022) 116162.

[6] M. Chatenet, B.G. Pollet, D.R. Dekel, F. Dionigi, J. Deseure, P. Millet, R.D. Braatz, M.Z. Bazant, M. Eikerling, I. Staffell, et al., Water electrolysis: from textbook knowledge to the latest scientific strategies and industrial developments, Chem. Soc. Rev. 51 (11) (2022) 4583–4762.

[7] M.B. Mogensen, M. Chen, H.L. Frandsen, C. Graves, A. Hauch, P.V. Hendriksen, T. Jacobsen, S.H. Jensen, T.L. Skafte, X. Sun, Ni migration in solid oxide cell electrodes: Review and revised hypothesis, Fuel Cells 21 (5) (2021) 415–429.

[8] V. Bilalis, X. Sun, H.L. Frandsen, M. Chen, Quantifying galvanostatic degradation of solid oxide electrolysis cells: The onset of accelerated degradation of Ni-yttria stabilized zirconia electrode, J. Power Sources 606 (2024) 234490.

[9] M. Trini, P.S. Jørgensen, A. Hauch, J. Bentzen, P. Hendriksen, M. Chen, 3D microstructural characterization of Ni/YSZ electrodes exposed to 1 year of electrolysis testing, J. Electrochem. Soc. 166 (2) (2019) F158.

[10] M. Trini, A. Hauch, S. De Angelis, X. Tong, P.V. Hendriksen, M. Chen, Comparison of microstructural evolution of fuel electrodes in solid oxide fuel cells and electrolysis cells, J. Power Sources 450 (2020) 227599.

[11] L. Rorato, Y. Shang, S. Yang, M. Hubert, K. Couturier, L. Zhang, J. Vulliet, M. Chen, J. Laurencin, Understanding the Ni migration in solid oxide cell: a coupled experimental and modeling approach, J. Electrochem. Soc. 170 (3) (2023) 034504.

[12] S.D. Ebbesen, C. Graves, A. Hauch, S.H. Jensen, M. Mogensen, Poisoning of solid oxide electrolysis cells by impurities, J. Electrochem. Soc. 157 (10) (2010) B1419.

[13] O.A. Marina, C.A. Coyle, E.C. Thomsen, D.J. Edwards, G.W. Coffey, L.R. Pederson, Degradation mechanisms of SOFC anodes in coal gas containing phosphorus, Solid State Ion. 181 (8–10) (2010) 430–440.

[14] M. De Ridder, A. Vervoort, R. Van Welzenis, H. Brongersma, The limiting factor for oxygen exchange at the surface of fuel cell electrolytes, Solid State Ion. 156 (3–4) (2003) 255–262.

[15] J.K. Nørskov, T. Bligaard, B. Hvolbæk, F. Abild-Pedersen, I. Chorkendorff, C.H. Christensen, The nature of the active site in heterogeneous metal catalysis, Chem. Soc. Rev. 37 (10) (2008) 2163–2171.

[16] J. Greeley, I. Stephens, A. Bondarenko, T.P. Johansson, H.A. Hansen, T. Jaramillo, J. Rossmeisl, I. Chorkendorff, J.K. Nørskov, Alloys of platinum and early transition metals as oxygen reduction electrocatalysts, Nat. Chem. 1 (7) (2009) 552–556.

[17] X.-K. Gu, E. Nikolla, Fundamental insights into high-temperature water electrolysis using Ni-based electrocatalysts, J. Phys. Chem. C 119 (48) (2015) 26980–26988.

[18] T. Ishihara, N. Jirathiwathanakul, H. Zhong, Intermediate temperature solid oxide electrolysis cell using LaGaO3 based perovskite electrolyte, Energy Environ. Sci. 3 (5) (2010) 665–672.

[19] O.I. Malyi, V.V. Kulish, K. Bai, P. Wu, Z. Chen, A computational study of the effect of alloying additions on the stability of Ni/c-ZrO2 interfaces, Surf. Sci. 611 (2013) 5–9.

[20] Z. Ouyang, A. Sciazko, Y. Komatsu, K. Nishimura, N. Shikazono, Influence of transition metal elements on Ni migration in solid oxide cell fuel electrodes, J. Electrochem. Soc. 170 (12) (2023) 124511.

[21] S. Zhang, N. van Dijk, S. van der Zwaag, A review of self-healing metals: Fundamentals, design principles and performance, Acta Met. Sin. (English Letters) 33 (2020) 1167–1179.

[22] N. van Dijk, S. van der Zwaag, Self-healing phenomena in metals, Adv. Mater. Interfaces 5 (17) (2018) 1800226.

[23] W. Xiong, H. Zhang, L. Vitos, M. Selleby, Magnetic phase diagram of the Fe–Ni system, Acta Mater. 59 (2) (2011) 521–530.

[24] G. Guisbiers, S. Khanal, F. Ruiz-Zepeda, J.R. De La Puente, M. José-Yacaman, Cu–Ni nano-alloy: mixed, core–shell or Janus nano-particle? Nanoscale 6 (24) (2014) 14630–14635.

[25] J. Enkovaara, C. Rostgaard, J.J. Mortensen, J. Chen, M. Dułak, L. Ferrighi, J. Gavnholt, C. Glinsvad, V. Haikola, H. Hansen, et al., Electronic structure calculations with GPAW: a real-space implementation of the projector augmented-wave method, J. Phys.: Condens. Matter. 22 (25) (2010) 253202.

[26] P.E. Blöchl, Projector augmented-wave method, Phys. Rev. B 50 (24) (1994) 17953.

[27] A.H. Larsen, J.J. Mortensen, J. Blomqvist, I.E. Castelli, R. Christensen, M. Dułak, J. Friis, M.N. Groves, B. Hammer, C. Hargus, et al., The atomic simulation environment—a Python library for working with atoms, J. Phys.: Condens. Matter. 29 (27) (2017) 273002.

[28] A.H. Larsen, M. Vanin, J.J. Mortensen, K.S. Thygesen, K.W. Jacobsen, Localized atomic basis set in the projector augmented wave method, Phys. Rev. B—Condens. Matter Mater. Phys. 80 (19) (2009) 195112.

[29] B. Hammer, L.B. Hansen, J.K. Nørskov, Improved adsorption energetics within density-functional theory using revised Perdew-Burke-Ernzerhof functionals, Phys. Rev. B 59 (11) (1999) 7413.

[30] A. Cadi-Essadek, A. Roldan, N.H. de Leeuw, Ni deposition on yttria-stabilized ZrO2 (111) surfaces: a density functional theory study, J. Phys. Chem. C 119 (12) (2015) 6581–6591.

[31] G. Henkelman, A. Arnaldsson, H. Jónsson, A fast and robust algorithm for bader decomposition of charge density, Comput. Mater. Sci. 36 (3) (2006) 354–360.

[32] M.C. Doppler, J. Fleig, M. Bram, A. Opitz, The capacitance of nickel pattern electrodes on zirconia electrolyte, J. Electrochem. Soc. 163 (10) (2016) H1019.

[33] M. Doppler, J. Fleig, M. Bram, A. Opitz, Hydrogen oxidation mechanisms on Ni/yttria stabilized zirconia anodes: Separation of reaction pathways by geometry variation of pattern electrodes, J. Power Sources 380 (2018) 46–54.

[34] M.Y. Lavrentiev, J. Wróbel, D. Nguyen-Manh, S. Dudarev, Magnetic and thermodynamic properties of face-centered cubic Fe–Ni alloys, Phys. Chem. Chem. Phys. 16 (30) (2014) 16049–16059.

[35] J. An, J.S. Park, A.L. Koh, H.B. Lee, H.J. Jung, J. Schoonman, R. Sinclair, T.M. Gür, F.B. Prinz, Atomic scale verification of oxide-ion vacancy distribution near a single grain boundary in YSZ, Sci. Rep. 3 (1) (2013) 2680.

[36] D. Kim, G. Dimitrakopoulos, B. Yildiz, Controlling the size of au nanoparticles on reducible oxides with the electrochemical potential, J. Am. Chem. Soc. 144 (48) (2022) 21926–21938.

[37] L. Li, X. Chang, X. Lin, Z.-J. Zhao, J. Gong, Theoretical insights into single-atom catalysts, Chem. Soc. Rev. 49 (22) (2020) 8156–8178.

[38] M.L. Weber, D. Jennings, S. Fearn, A. Cavallaro, M. Prochazka, A. Gutsche, L. Heymann, J. Guo, L. Yasin, S.J. Cooper, et al., Thermal stability and coalescence dynamics of exsolved metal nanoparticles at charged perovskite surfaces, Nat. Commun. 15 (1) (2024) 9724.

[39] Z. Ouyang, A. Sciazko, Y. Komatsu, N. Katsuhiko, N. Shikazono, Effects of transition metal elements on Ni migration in solid oxide cell fuel electrodes, ECS Trans. 111 (6) (2023) 171.

[40] H.H. Brongersma, M. Draxler, M. De Ridder, P. Bauer, Surface composition analysis by low-energy ion scattering, Surf. Sci. Rep. 62 (3) (2007) 63–109.

[41] A. Ruban, H.L. Skriver, J.K. Nørskov, Surface segregation energies in transition-metal alloys, Phys. Rev. B 59 (24) (1999) 15990.

[42] R. Kiebach, K. Norrman, C. Chatzichristodoulou, M. Chen, X. Sun, S.D. Ebbesen, M.B. Mogensen, P.V. Hendriksen, TOF-SIMS characterization of impurity enrichment and redistribution in solid oxide electrolysis cells during operation, Dalton Trans. 43 (40) (2014) 14949–14958.

[43] Y. Tao, J. Shao, S. Cheng, Electrochemically scavenging the silica impurities at the Ni–YSZ triple phase boundary of solid oxide cells, ACS Appl. Mater. Interfaces 8 (27) (2016) 17023–17027.

[44] R. Zollweg, Electron affinities of the heavy elements, J. Chem. Phys. 50 (10) (1969) 4251–4261.

[45] K.P. Kepp, A quantitative scale of oxophilicity and thiophilicity, Inorg. Chem. 55 (18) (2016) 9461–9470.

[46] Z. Jiao, N. Shikazono, Study on the effects of polarization on local morphological change of nickel at active three-phase-boundary using patterned nickel-film electrode in solid oxide fuel cell anode, Acta Mater. 135 (2017) 124–131.

[47] R. Knibbe, M.L. Traulsen, A. Hauch, S.D. Ebbesen, M. Mogensen, Solid oxide electrolysis cells: degradation at high current densities, J. Electrochem. Soc. 157 (8) (2010) B1209.